Self-emitted surface corrugations in dynamic fracture of silicon single crystal

Meng Wang, Marion Fourmeau, Lv Zhao, Franck Legrand, Daniel Nélias

Self-emitted surface corrugations in dynamic fracture of silicon single crystal

Meng Wang[a], **Marion Fourmeau**[a], **Lv Zhao**[b,c,1], **Franck Legrand**[a], **and Daniel Nelias**[a,1]

[a]Univ Lyon, INSA-Lyon, LaMCoS UMR CNRS 5259, F69621 Villeurbanne, France; [b]Department of Mechanics, Huazhong University of Science and Technology, Wuhan, 430074, China; [c]Hubei Key Laboratory of Engineering Structural Analysis and Safety Assessment, Wuhan, 430074, China

This manuscript was compiled on June 4, 2020

When dynamic crack front travels through material heterogeneities, elastic waves are emitted, which perturb the crack and change the morphology of fracture surface. For asperity-free crystalline materials, crack propagation along preferential cleavage planes is expected to present a smooth crack front and form a mirror-like fracture surface. Surprisingly, we show here that in single crystalline silicon without material asperities, the crack front presents a local kink during high-speed crack propagation. Meanwhile, local oscillations of the crack front, which can move along the crack front, emerge at the front kink position and generate periodic fracture surface corrugations. They grow from angstrom amplitude to few hundreds of nanometers and propagate with long lifetime at a frequency-dependent speed, while keeping a scale-independent shape. In particular, the local front oscillations collide in a particle-like manner rather than proceeding with a linear superposition upon interaction, which presents the characteristic of solitary waves. We propose that such propagating mode of the crack front, which results from the fracture energy fluctuation at a critical crack speed in the silicon crystal, can be considered as novel nonlinear elastic waves that we call 'corrugation waves'.

silicon single crystal | dynamic fracture | crack front kink | corrugation waves | solitary waves

Crack propagation is the main cause of catastrophic material failure. Although dynamic fracture has been intensively studied for decades, crack dynamics in crystalline materials still challenge our understandings (1, 2), as they are more complicated than that can be predicted by the classical theories on brittle crack propagation due to the inelastic phenomena at the atomic scale (3, 4). Linear elastic fracture mechanics (5) describe a crack tip in a two-dimensional medium as an energy sink, around which all dissipation processes occur during crack propagation. Crack speed v is determined through the balance between the energy flux into the crack tip G and the fracture energy $\Gamma(v)$ (energy needed to advance the crack tip of unit length at v). Regarding three-dimensional systems, crack front (the leading edge of the crack) should be considered. Local crack speed v_l at each point of the crack front is governed by local energy balance $\mathcal{G}_l = \Gamma_l(v_l)$, and the ensemble of local energy balances in turn controls the whole crack front shape (6, 7).

The crack front is generally stable and produces 'mirror-like' fracture surface under pure tension (8, 9). However, it may lose stability at high speed and generate 3D markings on fracture surface (10–14). A recent study (7) showed that the crack front can develop localized topological defects drifting along the front that lead to faceted fracture surfaces. Elastic waves also perturb the crack front and generate fracture surface undulations. Shear waves that propagate in the bulk solids have been shown to emit from material surface flaws and generate the well-known Wallner lines (15–19). Structural Lamb waves, generated upon debonding of implanted brittle layers and reflected from sample boundaries, can disturb the crack front and leave large scale periodic surface patterns (20). Moreover, a particular concept of one-dimensional elastic waves that exist only on the crack front, called crack front waves, emerged since the 1990s posterior to numerical predictions of persistent crack front oscillations caused by local heterogeneities of fracture energy in a linear elastic medium (6, 21–23). These waves propagate along the crack front at nearly the Rayleigh wave speed and locally change the in-plane and out-of-plane crack motion (24–26). Surface markings produced by the front waves were first reported in fracture tests on soda-lime glass incorporating artificial material asperities (27–29). Front wave traces emanated from both material asperities and crack micro-branching instabilities were observed (28, 29). Based on the post-mortem analysis of the fracture surface markings, the front waves were found to be solitary waves that are localized and long-lived. They present a unique scale-independent shape when scaling both the wavelength and the wave amplitude by the width of the initial perturbation, and exhibit a phase shift upon interaction (27). In this work, we report specific fracture surface corrugations in (110) cleavage of silicon single crystal, which only emerge in high-speed cracks. The corrugations initiate from local crack front kink and have a high correlation with the crack speed. Their morphology cannot be explained by any deflection scenario known for the (110) cleavage of silicon crystals. We propose that

Significance Statement

When moving crack front meets local material asperities, persistent nonlinear propagating mode of the crack front can be triggered, which results in non-trivial fracture surface patterns. Unexpectedly, we report continuous emergence of corrugation waves during high-speed crack propagation in asperity-free silicon single crystal. We reveal that these waves are driven by fracture energy fluctuation at critical crack speed. The corrugation waves are highly localized along the crack front. They twist the crack front and create fracture surface corrugations. Through meticulous quantitative characterization of the fracture surface markings, we evidence the nonlinear properties of these corrugation waves.

M.W., M.F., and F.L. performed the experiment and analyzed the data. M.W. and L.Z. carried out the finite element calculations. D.N. and L.Z. were involved in all aspects of the analysis of the results. All authors contributed to the writing of the manuscript.

The authors declare no conflict of interest.

[1]To whom correspondence should be addressed. E-mail: daniel.nelias@insa-lyon.fr, lvzhao@hust.edu.cn

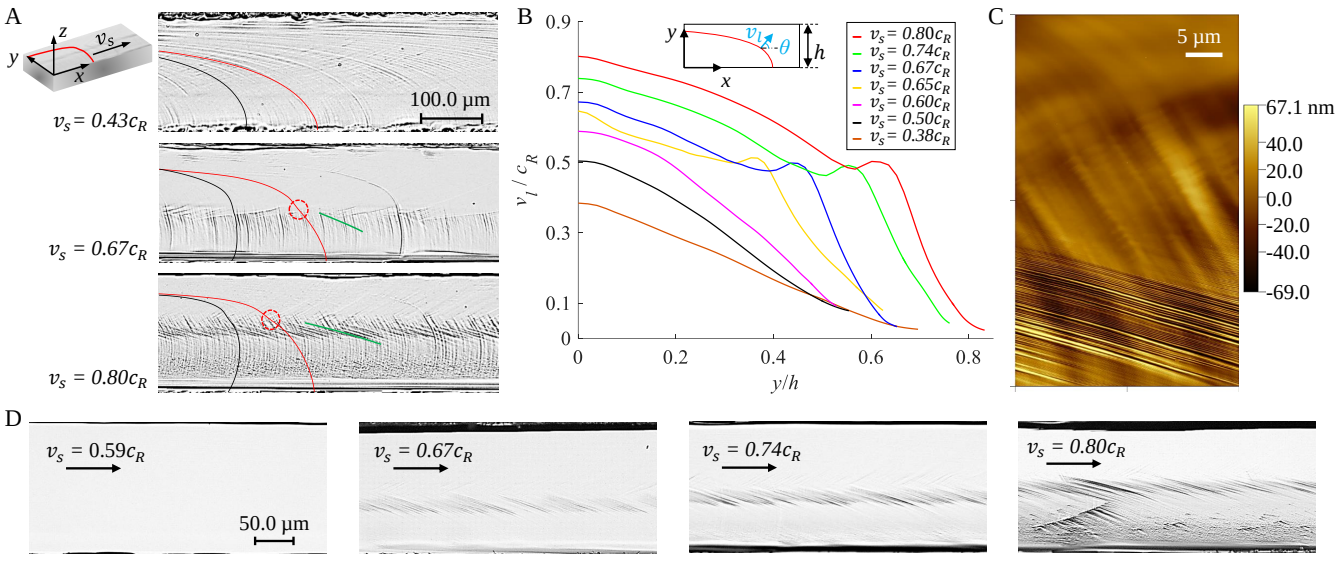

Fig. 1. Dynamic crack front behavior in steady-state (110) cleavage of the single crystalline silicon samples under pure bending. (*A*), Morphologies of the (110) cleavage plane (xy plane) of the as-sawn samples at different steady-state crack propagation speeds v_s. The crack propagates along the $[1\bar{1}0]$ direction (x axis). The Wallner lines and crack fronts are highlighted by the black and red curves, respectively. The local kinks of the crack front are highlighted by the red dashed circles and the surface corrugations are highlighted by the green lines. (*B*), Normalized local crack front speed v_l/c_R as a function of normalized vertical position y/h along the crack front, for seven experiments with different v_s. The inset illustrates the sample thickness h and the angle θ that represents the local normal direction of the crack front (red curve). (*C*), AFM measurement of the local front kink zone shows the emergence of the surface corrugations. (*D*), Morphologies of the (110) cleavage plane of the surface-polished samples at different v_s. Fracture surface morphologies exhibit the mirror-like feature at v_s = 0.59c_R, while the presence of surface corrugations at v_s = 0.67c_R (below 0.45h $\pm$ 0.01h), 0.74c_R (below 0.51h $\pm$ 0.02h) and 0.80c_R (below 0.59h $\pm$ 0.02h).

these self-emitted corrugations are traces of a new kind of nonlinear elastic waves, namely corrugation waves, that nucleate from the fracture energy fluctuation at a critical crack speed. The corrugation waves share certain properties with the crack front waves. We show, in addition to the scale-independent characteristic shape (27, 28), two intriguing attributes of the corrugation waves, i.e., nonlinear dispersion and particle-like interaction dynamics.

Result

Our fracture experiments were first performed on as-sawn single crystalline silicon plates under pure bending, which leads to the (110) cleavage (see Materials and Methods). Due to the bending stress gradient along the sample thickness, the local crack speed decreases from the bottom side to the top side and the leading front of the crack is curved. Note that the bending stress is normal to the fracture surface, the crack front thus propagates under pure opening mode (30). The crack front is found to rapidly accelerate to the steady-state regime (see SI *Appendix*, Texts S1-S2 and Figs. S1-S3), as also reported in refs.(19, 31–34). Thanks to various seed crack sizes, a wide range of steady-state crack speeds v_s, from 0.23c_R to 0.82c_R was obtained, where c_R represents the Rayleigh wave speed and is equal to 4460 m/s for the (110)$[1\bar{1}0]$ direction (35), allowing extensive examinations of crack dynamics. Fig. 1*A* shows the (110) cleavage surfaces at different v_s. Typical Wallner lines (black curves) generated from as-sawn surface flaws can be observed (see also SI *Appendix*, Text S3 and Fig. S4). The invariant shape of the Wallner lines reveals the steady-state propagation of the whole crack front. The crack front shape (red curves in Fig. 1*A*) is reconstructed via the retroactive decomposition of the Wallner lines (see SI *Appendix*, Text S4 and Fig. S5). It is found that, at $v_s < 0.62c_R$, the crack front exhibits a smooth quarter-ellipse shape, while it incorporates a local kink at higher speeds, as highlighted by the red circles in Fig. 1*A*. The front kink appears at an upper position along the crack front when v_s increases. Based on the steady-state crack front shape and speed, the local velocity at each point of the crack front v_l, assumed to be normal to the crack front, thus forming an angle θ relative to the x direction (insert in Fig. 1*B*), can be calculated as $v_s cos(\theta)$ (30, 31). The local crack speed profiles, normalized by anisotropic c_R for the (110) plane (35), are shown in Fig. 1*B*. In low-speed cases, v_l monotonically decreases from the bottom to the top along the crack front, while in high-speed cases, the local kink of the crack front is translated into a fluctuation in v_l, which takes place at around 0.5c_R, regardless of v_s.

When $v_s > 0.62c_R$, surface corrugations arise on the fracture surface, jointly with the crack front kink. As highlighted by the green lines in Fig. 1*A*, both the onset height and the orientation of these corrugations relative to the x direction have a strong dependency on the crack front speed (see SI *Appendix*, Text S2 and Figs. S2-S3 for more details). They nucleate at a nearly constant height during the steady-state crack propagation. Interestingly, the nucleation height rises with the increase of v_s, adhering to the local front kink position (see Fig. 1*C* and SI *Appendix*, Fig. S2-S3), where v_l fluctuates at around 0.5c_R. Therefore, the crack front kink, the v_l fluctuation and the appearance of surface corrugations are coupled, crack speed-dependent events in high-speed cracks.

To study accurately the morphological features of the fracture surface corrugations, a second experimental campaign was carried out on surface polished silicon samples to exclude the Wallner lines (see Materials and Methods). Fig. 1*D* shows the mirror-like fracture surface at $v_s = 0.59c_R$ and corrugated fracture surfaces at $v_s = 0.67c_R$, 0.74c_R and 0.80c_R for the pol-

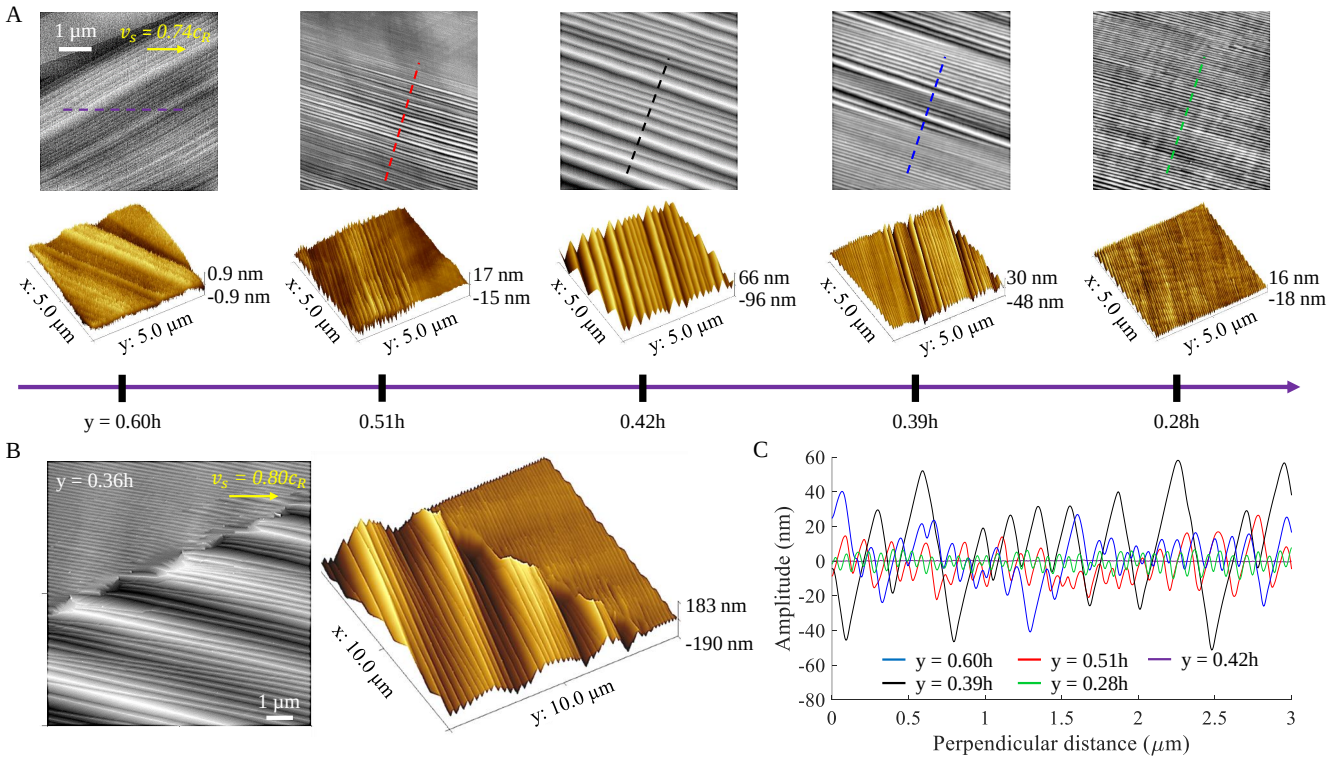

Fig. 2. AFM measurement of the fracture surface corrugations in the polished single crystalline silicon samples. (*A*), Topographies of the surface corrugations at v_s = 0.74c_R at different heights. (*B*), Collapse of previous corrugations and emergence of new ones at high-speed crack instabilities at v_{fo} = 0.80c_R. (*C*), Profiles of the surface corrugations (along the perpendicular direction of the corrugation ridge) at different life stages at v_s = 0.74c_R. The profiles were extracted along the dashed lines highlighted in (*A*) with the corresponding colors.

ished samples. The onset position of corrugations still adheres to the crack front kink (see SI *Appendix*, Fig. S2). Note here that the surface corrugations on the two opposing fracture surfaces involve a peak-to-valley match (see SI *Appendix*, Fig. S6). This should be distinguished from the particular nanoscale corrugations resulting from local plasticity ahead the crack tip which presents a peak-to-peak match (36). Nanoscale topographies of the surface corrugations are analyzed via the atomic force microscope (AFM) measurements. Fig. 2*A* shows five typical topographies at $v_s = 0.74c_R$ for different locations along y (the definition of y is given in the inset of Fig. 1*A*). At $y = 0.6h$, the fracture surface is flat and contains only sub-nano atom debonding lines pointing towards the upper side of the sample. The surface corrugations nucleate at $y = 0.51h \pm 0.02h$, which corresponds to the local front kink position. Their amplitudes grow from an angstrom level ($y = 0.51h$) to a maximum of roughly hundred nanometers ($y = 0.42h$). Outside the front kink zone ($y = 0.39h$), the corrugations rapidly decay in both amplitude and width. After the decay (below $y = 0.35h$), the surface corrugations extend at a nearly constant amplitude of about 10 nm with long lifetime, till the bottom of the fracture surface.

In particular, Fig. 2*B* highlights the occurrence of high-speed crack instability, which induces an abrupt crack path deviation and extends along the local front normal direction (see SI *Appendix*, Text S5 and Fig. S7 for more details). In this region, previous corrugation markings collapse and new single or multiple corrugation markings arise along the instability line. Their amplitudes are maximum upon nucleation (the amplitude evolution is detailed in SI *Appendix*, Fig. S8). The surface corrugations all exhibit wave-like feature along the perpendicular direction of the corrugation ridge, as shown in Fig. 2*C*. The angle between the corrugation planes, denoted by β, is measured to further reveal the geometrical characteristics of the corrugations. Fig. 3*A* highlights the β distribution at different life stages for $v_s = 0.74c_R$. The mean value of β is about 137° at the nucleation stage of the corrugations. It then decreases to approximately 135° during the growth and finally increases to 140° after the decay of the corrugations. Fig. 3*B* shows the dependency of β, measured in the zone presenting the maximum amplitude of the surface corrugations, on the crack speed v_s. It can be noticed that β decreases with the increase of v_s (the distributions of β for $v_s = 0.67c_R$ and $0.80c_R$ at different locations are shown in SI *Appendix*, Fig. S9). Moreover, the surface corrugations extend along various crystallographic directions depending on the crack speed (see SI *Appendix*, Figs. S2-S3). Therefore, one can conclude that the surface corrugations do not coincide with any specific crystal plane.

It is noteworthy that specific surface patterns, called facets, were also reported in the (110) cleavage of silicon crystal under tension when the crack speed exceeds $0.67c_R$ (9). These facets appear in the mirror-like zone of the fracture surface and clearly lie on {111} planes towards the end of the mirror zone when the crack speed is high. They display hills and valleys with a length-scale of 100-1000 nm, which are similar to the surface corrugations in the present study. However, the facets reported in ref.(9) extend only in the $[1\bar{1}0]$ direction throughout the fracture surface, regardless of the crack speed. This is well different from the surface corrugations shown

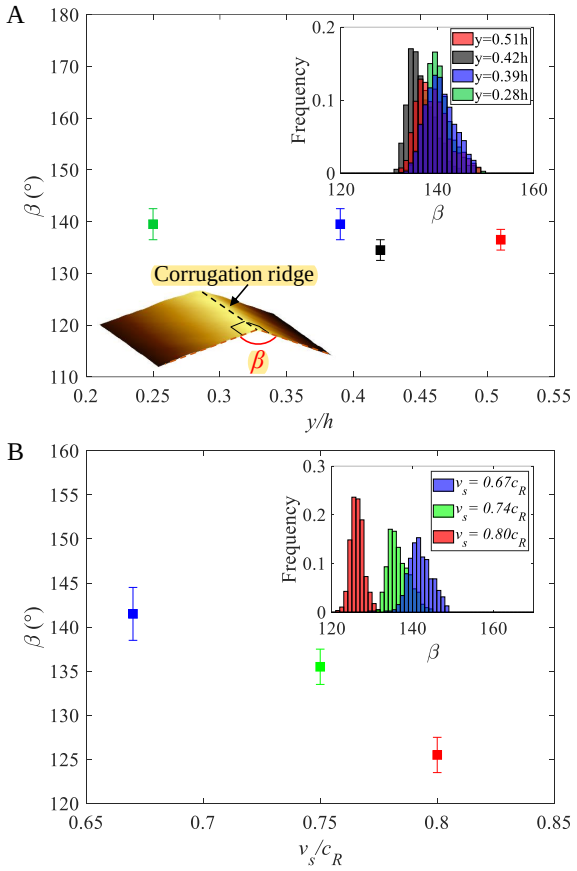

Fig. 3. Distribution of angle β between corrugation planes. (*A*), Variations of β as a function of the normalized vertical position y/h at v_s = 0.74c_R. The mean values of β and the standard deviations were determined from the histograms of β shown in the inset on the top right, which were computed from the profiles of the corrugations measured perpendicular to the corrugation ridge at different life stages presented in Fig. 2*A*. Schematic drawing of β is shown in the inset on the bottom left. (*B*), Dependency of β on v_s. The mean values of β and the standard deviations were determined from the histograms of β shown in the inset, computed from the profiles of the corrugations measured perpendicular to the corrugation ridge in the zone where the corrugations extend with the maximum amplitude at different v_s.

here, of which both the nucleation position and the extending direction exhibit a strong dependency on the crack front speed. Moreover, the surface corrugations do not coincide with the {111} planes even when $v_s = 0.80c_R$ (the comparison of the geometry between the surface corrugations and the {111} facets is presented in SI *Appendix*, Fig. S10). Hence, the surface corrugations are different from the facets reported in ref.(9). The long-lived propagation with a well-defined shape of the surface corrugations (which extend over four decades and keep a nearly invariant shape with an amplitude of one decade) reveals that they are generated by highly localized out-of-plane perturbations along the crack front, i.e., the local crack front oscillations.

The characteristics of the local crack front oscillations are assessed with the periodic surface corrugations. As illustrated in Fig. 4*A*, when the front oscillations propagate at speed v_{fo}, they generate surface corrugations oriented with an angle α relative to the x direction. As the surface corrugations are the traces of the front oscillations, their profiles along the crack front therefore provide the shape of the front oscillations (wavelength λ_{fo} and amplitude A_{fo}). When extracting λ_{fo} and A_{fo}, we assume that the crack front is smooth at the length scale of the surface corrugations, hence the front tangent coincides with that of the crack front reconstructed at the length scale of the Wallner lines. It is found that the orientation of the corrugations α changes with the wavelength λ_{fo}. Figs. 4*B-D* show that α increases (decreases) when the width of the corrugations increases (decreases), as highlighted by the yellow and red arrows. This dependence can be observed during both the growth (see Fig. 4*B*) and the decay (see Fig. 4*C*) of the corrugations, as well as upon nucleation of new corrugations triggered by high-speed crack instabilities (see Fig. 4*D*). Moreover, α is constant for corrugations of large width, as highlighted by the green arrows in Fig. 4*B*. Given that the speed of the local front oscillations v_{fo} is related to α through $v_{fo} = v_l/\cos(\alpha+\theta)$, the correlation between α and λ_{fo} can be translated into the relation between v_{fo} and λ_{fo}. As shown in Fig. 4*E*, for $\lambda_{fo} > 220$ nm, v_{fo} is approximately equal to the Rayleigh wave speed. However, for $\lambda_{fo} < 220$ nm, v_{fo} significantly drops when λ_{fo} decreases, indicating the dependence of v_{fo} of the front oscillation on its frequency. This dependence can be characterized by the frequency of the front oscillations ω_{fo} (given by $2\pi v_{fo}/\lambda_{fo}$) as a function of the wavenumber (given by $2\pi/\lambda_{fo}$). The relation becomes nonlinear above $\omega_{fo} = 1.23 \times 10^{11}$ rad/s (inset of Fig. 4*F*).

Furthermore, during the growth (decay) of the crack front oscillations, we reveal that λ_{fo} increases (decreases) when A_{fo} increases (decreases). As a result, sparser corrugations exhibit larger amplitude (see the AFM measurements in Fig. 2*C*). To further quantify the relationship between λ_{fo} and A_{fo}, the shapes of the front oscillations are extracted from the surface corrugations at $v_s = 0.80c_R$, in the region where y varies between $0.46h$ and $0.36h$ (i.e., θ varies between 42° and 33°). The corresponding shapes of the front oscillations are plotted in Fig. 4G. It can be noticed that λ_{fo} exhibits approximately a linear correlation with A_{fo} (see inset, Fig. 4*G*). Interestingly, the local front oscillations present a scale-independent characteristic shape upon normalization over A_{fo} and λ_{fo} (see Fig. 4*H*). It should be noted that the characteristic shape is not affected by the lattice structure of the silicon crystal, given that the front oscillations travel on the anisotropic (110) crystal plane.

In addition to the frequency-dependent speed and the scale-independent shape, we report another property of the local front oscillations, which is reflected by their particle-like interaction behavior. As can be appreciated in Figs. 5*A* and *B*, when a fast moving oscillation (long λ_{fo}) meets a slow one (short λ_{fo}), they exhibit a particle-like collision. The interaction scenario highlighted here is that the fast moving oscillation decays and decelerates while the slow one grows and accelerates (see Fig. 5*B*). It is noteworthy that the linear correlation between λ_{fo} and A_{fo} is retained, hence the shape of the front oscillation remains scale-independent during the interaction. After the collision, both the shape and the speed of the front oscillations exchange and an orientation shift occurs for the surface corrugations involved in the interaction. The collision events are more frequent when successive interactions of the crack front oscillations take place. As shown in Figs. 5*C-D*, alternative growth (acceleration) and decay (deceleration) of the front oscillations occur during the consecutive collisions, which generate the surface corrugations with repeated variations in orientation and amplitude.

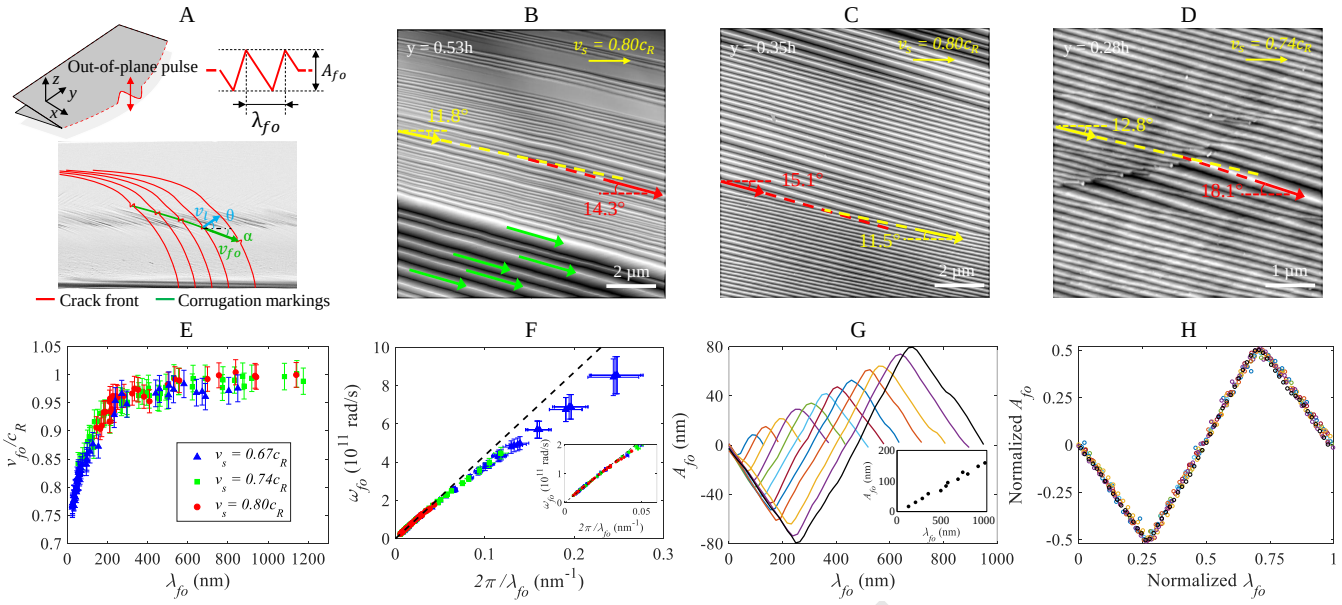

Fig. 4. Characterization of local crack front oscillations. (*A*), Local crack front oscillations with the out-of-plane amplitude A_{fo} and wavelength λ_{fo} are localized along the crack front (red curve), propagate at v_{fo}, and leave corrugation markings forming an angle α relative to the x direction. λ_{fo} is defined as the distance between two adjacent crests of the periodic oscillations. (*B*)-(*D*), Dependency of the tilt angle α of the corrugation markings at different life stages when $\lambda_{fo} < 220$ nm. The variations of α are highlighted by the yellow and red lines. (*B*), The growth of the corrugation markings shows the increase of α with the increase of λ_{fo}. The green arrows highlight that corrugation markings with $\lambda_{fo} > 220$ nm present constant α. (*C*), The decay of the corrugation markings shows the decrease of α with the decrease of λ_{fo}. (*D*), The new corrugation markings with longer λ_{fo} triggered by the high-speed crack instabilities show larger α in comparison to previous markings. (*E*), The normalized speed of front oscillations v_{fo}/c_R as a function of the wavelength λ_{fo}. (*F*), The frequency of local front oscillations ω_{fo} as a function of the wavenumber $2\pi/\lambda_{fo}$. The linear relation is highlighted by the black dashed line. A zoom of the linear part with $\omega_{fo} < 1.23 \times 10^{11}$ rad/s is highlighted in the inserted graph. The uncertainties of v_{fo} and λ_{fo} result from the v_s measurement by the high-speed camera and the surface marking measurement by the AFM. (*G*), Shape of the front oscillations. The shapes with A_{fo} varying between 16.6 nm and 159.6 nm were extracted from the AFM measurements along the crack front at $v_s = 0.80c_R$. The inset shows the linear correlation between the amplitude A_{fo} and the wavelength λ_{fo} of front oscillations. (*H*), Scale-independent characteristic shape of the local front oscillations. The shapes of front oscillations are normalized over their amplitudes and wavelengths, i.e., the abscissa and the ordinate are normalized by λ_{fo} and A_{fo}, respectively.

Discussion and conclusion

Why the crack front locally kinks and the local crack speed fluctuates when $v_s > 0.62c_R$? According to the linear elastic fracture mechanics, the local energy balance for each point y of a propagating mode I crack front reads (6):

$$\mathcal{G}_l[\{F(y',t' \leqslant t)\},y,t] = \Gamma_l[x = F(y,t),y] \qquad [1]$$

The region $x < F(y,t)$ represents the crack wake and $x = F(y,t)$ corresponds to the current crack front. The coordinates x and y are the same as in Fig. 1*A*. The local energy flux $\mathcal{G}_l$ depends on the crack velocity as well as the history of the whole crack front $\{F(y',t' \leqslant t)\}$. The local energy flux $\mathcal{G}_l$ is given by the general form:

$$\mathcal{G}_l = G_l[\{F(y',t' < t)\},y,t]g(v_l) \qquad [2]$$

with

$$g(v_l) \simeq 1 - v_l/c_R \qquad [3]$$

where G_l is the local strain energy release rate at (y,t) for a crack at rest, which is independent of the crack velocity, and v_l is the local velocity normal to the crack front. In our case, since we only consider the crack propagation at a steady-state speed v_s with an invariant shape $F^*(y)$, $F \to F + \delta F = F^*(y) + v_s t$. The dependency of G_l on the front history $\{F\}$ vanishes. The local energy balance can be simplified as:

$$\Gamma_l[F^*(y) + v_s t,y] = G_l^s[F^*(y) + v_s t,y]g(v_l) \qquad [4]$$

where G_l^s is the static local strain energy release rate that can be determined at a given moment $t = t_0$ with the cracked sample geometry $F^*(y) + v_s t_0$ and the applied load.

Equation. (4) implies that the v_l fluctuation related to the front kink at the high-speed crack front should be the response to an abnormal variation in Γ_l. To verify this conjecture, the instantaneous G_l^s was computed using 3D finite element simulations where the real steady-state crack front shapes and the experimental conditions were considered (see SI *Appendix*, Text S7 and Fig. S11). Only the crack front at the very beginning of the steady-state regime was taken into account, where t_0 was very small since the crack accelerates very rapidly to the steady state, as reflected by the invariant Wallner lines (see SI *Appendix*, Fig. S3*C*). Hence, the stress field ahead of the crack front would not be affected by the stress waves reflected from the sample boundaries (see SI *Appendix*, Text S7), and Eq. (4) therefore remains valid, as also proposed in ref.(5). Moreover, as we just consider the steady-state crack propagation at very small t_0, the applied load at $t = t_0$ could be assumed to be the same as that at the crack initiation. The local fracture energy Γ_l is then calculated using Eq. (4) with the known v_l (Fig. 1*B*), G_l^s (SI *Appendix*, Fig. S11*E*) and c_R (35).

Seven cracks with v_s varying from $0.38c_R$ to $0.80c_R$ are analyzed. Normalized Γ_l (over Γ_0 that represents 2 times the surface energy) along the crack front is displayed in Fig. 6*A*. One can see that Γ_l is almost constant for $v_s < 0.60c_R$, while it significantly increases at certain height for $v_s > 0.65c_R$. In particular, the jump occurs at higher position for larger

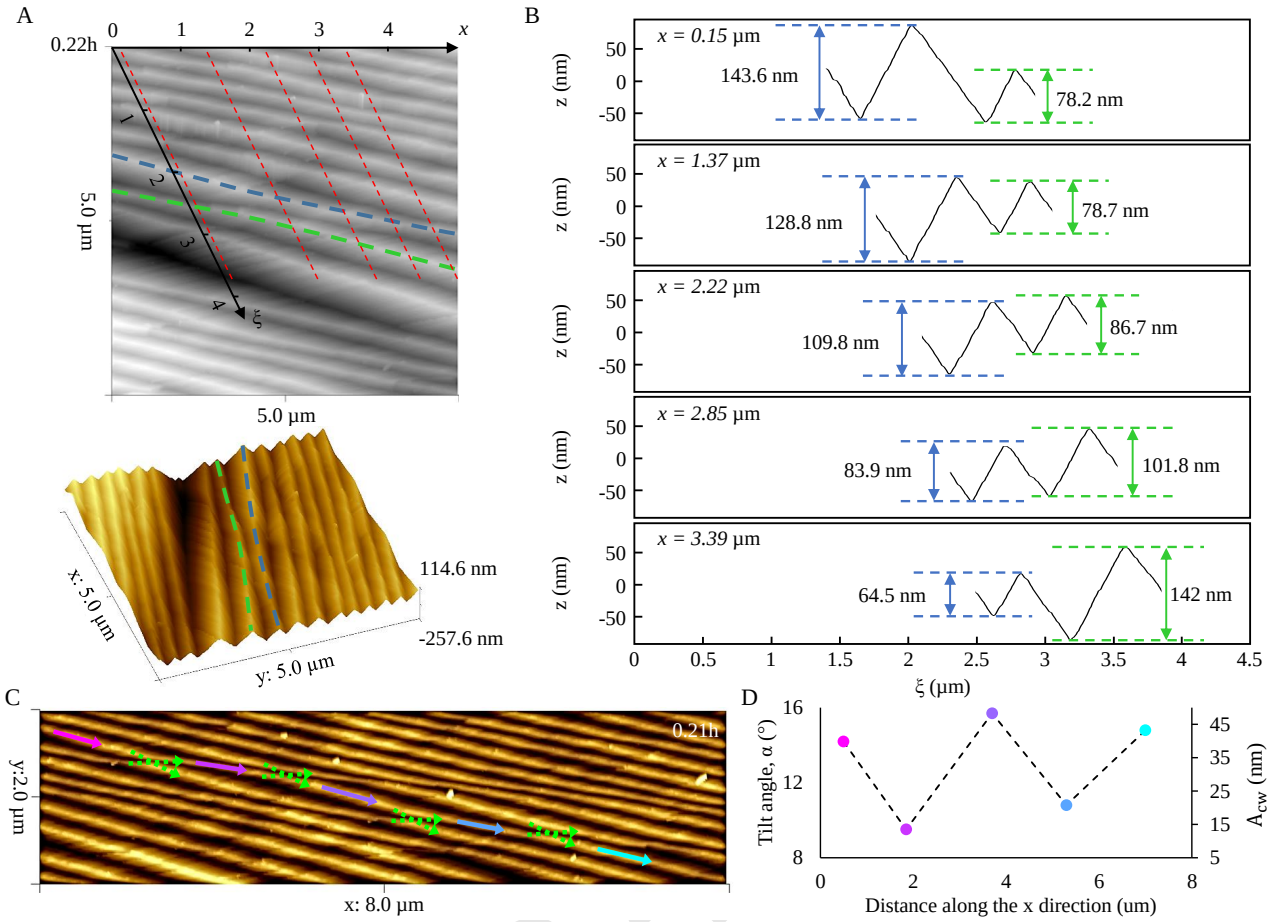

Fig. 5. Collision behavior of crack front oscillations. (*A*), Topographies of the surface corrugations at v_s = 0.80 c_R. The ξ axis is the tangent direction of the crack front. Corrugation markings generated by the collision of front oscillations, as highlighted by the blue and green dashed lines, respectively. The corrugation markings exchange their orientation α after the collision. (*B*), Sequences of shape evolution of the front oscillations during the collision mentioned in (*A*). The five sequences along the x direction are highlighted in (*A*) by the red dashed lines. At x = 0.15 μm, different front oscillations propagate at v_{fo} = 0.965c_R (blue) and v_{fo} = 0.935c_R (green), respectively, then they exchange their speeds at x = 3.39 μm. (*C*), Topographies of the surface corrugations at v_s = 0.74 c_R, y = 0.21h incorporating successive collisions that result in successive phase shifts, as highlighted by the green dashed arrows. (*D*), Simultaneous variation of α and A_{fo} of the corrugation marking generated by successive collisions of front oscillations, measured from the arrows with the corresponding colors in (*C*).

v_s, which coincides with the crack front kink as well as the onset of the corrugation markings. When plotting Γ_l as a function of v_l along various crack fronts (see SI *Appendix*, Fig. S12), we find that Γ_l involves a jump at v_l of about $0.5c_R$. This corresponds well to the fact that v_l fluctuates at $0.5c_R$ whatever the global crack speed (see Fig. 1*B*). Moreover, the numerous crack fronts provide a possibility to assess Γ_l versus v_l for a given crystallographic direction, which can be analogue to the straight tensile crack scenario. Fig. 6*B* shows Γ_l for the $[1\bar{1}1]$, $[2\bar{2}1]$ and $[1\bar{1}0]$ directions, represented by the blue, green and black marks, respectively. One can see that Γ_l is nearly equal to the initiation fracture toughness 2γ (3, 37), when v_l is low. It then jumps at a critical speed v_c, which depends on the crystallographic direction. For instance, v_c is about $0.50c_R$ for the $[1\bar{1}1]$ direction and $0.60c_R$ for the $[1\bar{1}0]$ direction, which are in excellent agreement with refs.(4, 38) (see SI *Appendix*, Fig. S12), and $v_c = 0.58c_R$ for the $[2\bar{2}1]$ direction is for the first time presented here.

With the characteristic shape of the front oscillations, we assess that the increase of the fracture surface due to the surface corrugations is about 6%, which is much lower than the increase in Γ_l. No subsurface crack was found under the surface corrugations (see SI *Appendix*, Fig. S13). Therefore, we may adhere to the conjecture made in ref.(9), recently proved by molecular dynamics simulations (4, 38), that the sharp increase in dynamic fracture energy in silicon crystal results from the additional dissipation by phonon emission, which is also found to depend on the crystallographic structure of the silicon crystal. For the crack front containing the local crack speed gradient, the increase in Γ_l induced by phonon emission occurs along the front portion where $v_l \geq v_c$, while $\mathcal{G}_l$ is equal to 2γ for the rest of the front where $v_l < v_c$. The jump in Γ_l takes place at the location where $v_l = v_c$. The critical speed v_c is found to be about $0.5c_R$ for the local crystallographic direction θ varying between 30° and 50°, and it changes for other directions, which is in agreement with the anisotropic dissipation of the phonon emission revealed in ref.(4, 38) (see Fig. 6*B* and SI *Appendix*, Fig. S12). Indeed, a sharp increase in Γ_l will locally slow down the crack front and the resulting fluctuation in v_l consequently produces a kink of the crack front. Note that all material-dependent, dissipative processes are embraced in Γ_l, we point out that the local fracture energy jump induced by the phonon emission and the consequent crack front kink can be well interpreted through local energy

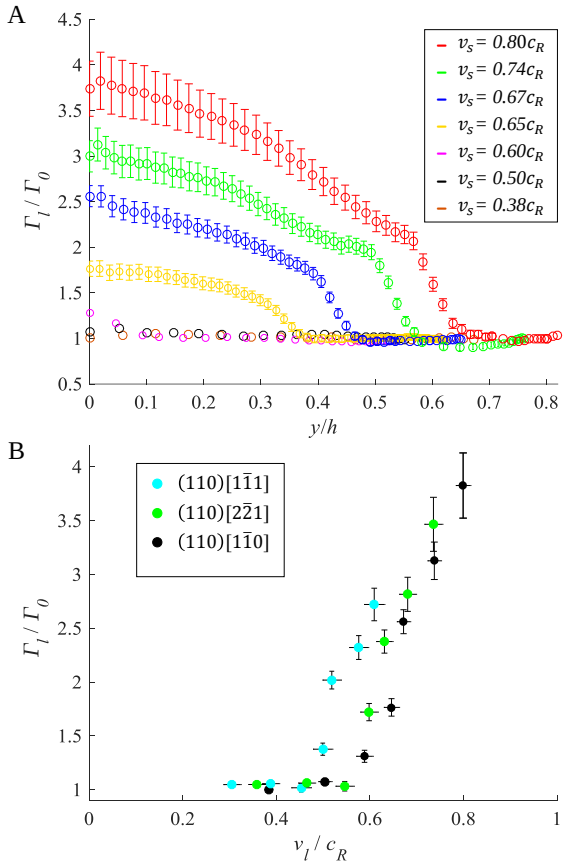

Fig. 6. (*A*), Variation of the normalized local dynamic fracture energy Γ_l/Γ_0 along the crack front as a function of y/h, for the same seven fracture cases as in Fig. 1*B*)) with the corresponding colors. (*B*), Γ_l/Γ_0 versus v_l/c_R along the $[1\bar{1}1]$, $[2\bar{2}1]$ and $[1\bar{1}0]$ directions, presented by the blue, green and black marks.The error bars are obtained from the uncertainties in the crack speed measurements.

balances $\mathcal{G}_l = \Gamma_l(v_l)$ in the framework of LEFM.

The local fracture energy jump reported here is supposed to induce only an in-plane fluctuation of local crack speed and consequently alter the planar crack front dynamics. Nevertheless, it breaks down the translational invariance of the moving front and induces abnormal gradient of the energy flux $d\mathcal{G}_l/dy$ at the front kink site. As suggested by theoretical predictions and experimental observations, the abnormal $d\mathcal{G}_l/dy$ fulfills the nucleation condition of crack front waves (6, 21, 29). Therefore, the emission of the fracture surface corrugations at the Γ_l jump zones indicates that the front oscillations share the generation condition with the front waves, i.e., local fracture energy fluctuation ahead of the crack front. We conjecture that, like the out-of-plane corrugations (24) and the front waves (39), any slight out-of-plane perturbation (for instance the sub-nano atom debonding lines, see Fig. 2*A*) could trigger the out-of-plane component of the front oscillations which sprouts from the atomic scale.

Since the local front oscillations can travel along the crack front, they present a propagating mode of the crack front. This propagating mode can not be considered as the front waves, as they propagate approximately at the Rayleigh wave speed only for the large length scale ($\lambda_{fo} > 220$ nm). We suggest that the frequency-dependent speed for $\omega_{fo} > 1.23 \times$ rad/s 10^{11} is due to the nonlinear dispersion of the front oscillations (40, 41). Nevertheless, the unique characteristic shape of the front oscillations coincides with the property of the front waves (27). It reveals an intrinsic nonlinear attribute of the front oscillations. This is well distinguished from the undulation of the crack front induced by linear elastic waves, for which the wavelength is independent of the amplitude. Taking the Wallner lines (note that the Wallner lines are commonly believed to be generated by shear waves) observed in the as-sawn samples for comparison, it is found that the shear waves nucleated at the surface flaws exhibit a constant wavelength, as reflected by the constant width of the Wallner lines during their decay (see SI *Appendix*, Fig. S4). Besides, the shape of the shear wave packets is found to depend on the generation source and exhibits no well-defined nature (29) (see also SI *Appendix*, Fig. S4). Furthermore, the collision events reveal another nonlinear attribute of the front oscillations. Instead of a linear superposition as the linear elastic waves would proceed, the particle-like interaction of the front oscillations is similar to the collision of solitary waves, during which the two pulses exchange their speeds and shapes, resulting in a phase shift (27, 29, 42). Hence, we conclude that the front oscillations reported in this work, which share certain properties with crack front waves, can be considered as nonlinear elastic waves. We call them 'corrugation waves' since they produce periodic out-of-plane corrugations on the fracture surface.

The corrugation waves deform the crack front and lead to an increase of the fracture surface. They create extra energy dissipations and hence can propagate only in the region when $\mathcal{G}_l > 2\gamma$. On the upper side of the nucleation site of the corrugation waves, $\mathcal{G}_l = 2\gamma$ (see Fig. 6*A*). Therefore, no additional energy can support the corrugation waves to extend to the upper side. This explains why the corrugation waves extend solely to the lower side where $\mathcal{G}_l > 2\gamma$. The most distinguishable behavior of the corrugation waves reported here is that they are continuously self-emitted from the moving front and propagate with the characteristics of solitary waves. As a result, periodic surface corrugations are created and cover the whole fracture ligament, as experimentally observed. The continuous nucleation of corrugation waves in response to the fracture energy jump at the critical crack speed could be analogous to the consequence of a crack traveling through substantial heterogeneities, which continually twist the crack front (43, 44). The initial state of the corrugation waves depends on the source that creates them. The gradual growth of corrugation waves at the front kink zone (Fig. 2*A*) could be explained by the continuous increase in the fracture energy (see Fig. 6*A*), while the corrugation waves incorporating the maximum amplitude upon emission is due to the abrupt change in fracture energy caused by the high-speed crack instabilities (see Fig. 2*B*).

In summary, the nonlinear attributes of the corrugation waves reported here, such as the scale-independent characteristic shape, the nonlinear dispersion and the particle-like collision construct a new propagating mode of crack front, which is different from what has been described for the front waves with the numerical modeling and experiments incorporating individual material asperities. Our results may give new insights on soliton-like crack front dynamics, as well as roughness formation on the fracture surface of asperity-free crystalline materials.

Materials and Methods

Silicon sample preparation. Solar-grade single crystalline silicon wafer with a purity of 99.9999% was used. We prepared two types of silicon samples: as-sawn silicon samples and mirror-polished silicon samples. (001) silicon wafers were cut by diamond wire from boron-doped single crystalline silicon ingot with a dopant concentration of 5.44×10^{15} atoms/cm^3. The error in sawing direction relative to the (001) plane is 3°. The damaged surface of wafers was cleaned up by chemical etching to remove a thin layer, but the wire sawing flaws were partially kept. As-sawn silicon samples of size $50 \times 50 \times 0.19$ mm^3 were obtained by cleavage from the (001) silicon wafers. For preparing mirror-polished silicon samples, a layer of 10 μm was eliminated by mechanical polishing for both surfaces of the (001) silicon wafers. Mirror-polished silicon samples of $50 \times 30 \times 0.17$ mm^3 were then cleaved from the polished silicon wafers. The single crystal for all the samples is oriented such that the sample surface is perpendicular to the [001] direction and the two edges are parallel to the <110> directions.

Fracture experiments. 100 experiments, including 70 on as-sawn silicon samples and 30 on mirror-polished silicon samples were carried out to ensure the reliability of the experimental results. The samples were loaded under four-line bending condition along the [110] direction (y direction) via quasi-static displacement at a strain rate of 10^{-6} s^{-1}. The spans of the punch roller and the support are 21 mm and 40 mm, respectively. A single crack that propagates on the (110) plane was driven from a seed crack introduced at the center of the sample edge using a Vickers indenter. The indentation force was well controlled to obtain a sharp seed crack of desired length located on the (110) plane. Fracture process of the bottom surface of the sample was captured with a high-speed camera (Phantom V710). For as-sawn silicon samples, we recorded images with a spatial resolution of 97.6 μm/pixel and an acquisition rate of 180,000 frames per second. For mirror-polished silicon samples, we recorded images at a spatial resolution of 89.3 μm/pixel and an acquisition rate of 340,000 frames per second (the acquisition rate can be increased when the image window is reduced to match the sample dimension). The crack position was identified by the gradient of light intensity resulting from the curvature variation around the crack tip, as the sample was illuminated by a continuous light source (MultiLED G300). The uncertainties on crack speed measurement are 70 m/s and 121 m/s for as-sawn and mirror-polished samples, respectively, since we took an uncertainty of 4 pixels on the crack tip location.

Post-mortem analysis of fracture surface. The fracture surfaces of all the tested samples were observed with a digital microscope (Keyence VHX-2000). The fracture surface morphologies are almost identical for similar steady-state speed. The Wallner lines were intensive for the as-sawn samples and few could be seen for the polished samples as surface defects were not completely removed. Their shapes can be strikingly observed and then be extracted after contrast enhancement of fractography. The 3D topographies of the fracture surfaces of mirror-polished samples were measured using AFM (Bruker Dimension 3100 Nanoscope V) with an out-of-plane (along z direction) resolution of 0.1 nm. The silicon sample was aligned in the AFM setup so that the edge of the fracture surface was parallel to one line of the crosshair. The misalignment error is in the order of ±0.5°. The measurements were carried out in a square region of 5×5 μm^2, 10×10 μm^2 or 20×20 μm^2, corresponding to an in-plane (xy plane) resolution of 5 nm, 10 nm or 20 nm, respectively. Each direction was scanned back and forth to ensure that there was no bias due to the scanning direction and the speed of the AFM tip. The analysis of AFM measurements was carried out with the Gwyddion software (45).

Data Availability. All materials, methods and data supporting the findings of this study are available within the paper and SI *Appendix*. The AFM measurement of the surface corrugation markings, custom Matlab code for the crack front reconstruction and the finite element model reported in this work have been deposited in Zenodo: https://doi.org/10.5281/zenodo.3601407

ACKNOWLEDGMENTS. This research was supported by the French research agency ANR (Grant number: ANR-11-EQPX-0014) through the DURASOL Equipex project. We thank D. Albertini for his kind help on the AFM measurements, and we thank A. Gravouil, A. Tanguy and T. Albaret for fruitful discussions.

1. BN Cox, H Gao, D Gross, D Rittel, Modern topics and challenges in dynamic fracture. *J. Mech. Phys. Solids* **53**, 565–596 (2005).
2. E Bouchbinder, T Goldman, J Fineberg, The dynamics of rapid fracture: instabilities, nonlinearities and length scales. *Reports on Prog. Phys.* **77**, 046501 (2014).
3. R Pérez, P Gumbsch, Directional anisotropy in the cleavage fracture of silicon. *Phys. review letters* **84**, 5347 (2000).
4. F Atrash, A Hashibon, P Gumbsch, D Sherman, Phonon emission induced dynamic fracture phenomena. *Phys. review letters* **106**, 085502 (2011).
5. LB Freund, *Dynamic fracture mechanics*. (Cambridge university press), pp. 296–437 (1998).
6. S Ramanathan, DS Fisher, Dynamics and instabilities of planar tensile cracks in heterogeneous media. *Phys. Rev. Lett.* **79**, 877 (1997).
7. I Kolvin, G Cohen, J Fineberg, Topological defects govern crack front motion and facet formation on broken surfaces. *Nat. materials* **17**, 140 (2018).
8. S Ramanathan, D Ertaş, DS Fisher, Quasistatic crack propagation in heterogeneous media. *Phys. review letters* **79**, 873 (1997).
9. T Cramer, A Wanner, P Gumbsch, Energy dissipation and path instabilities in dynamic fracture of silicon single crystals. *Phys. Rev. Lett.* **85**, 788 (2000).
10. J Fineberg, SP Gross, M Marder, HL Swinney, Instability in dynamic fracture. *Phys. Rev. Lett.* **67**, 457 (1991).
11. M Marder, X Liu, Instability in lattice fracture. *Phys. Rev. Lett.* **71**, 2417 (1993).
12. E Sharon, J Fineberg, Microbranching instability and the dynamic fracture of brittle materials. *Phys. Rev. B* **54**, 7128 (1996).
13. A Livne, O Ben-David, J Fineberg, Oscillations in rapid fracture. *Phys. review letters* **98**, 124301 (2007).
14. CH Chen, E Bouchbinder, A Karma, Instability in dynamic fracture and the failure of the classical theory of cracks. *Nat. Phys.* **13**, 1186 (2017).
15. H Wallner, Linienstrukturen an bruchflächen. *Zeitschrift für Physik* **114**, 368–378 (1939).
16. J Field, Brittle fracture: its study and application. *Contemp. Phys.* **12**, 1–31 (1971).
17. D Bonamy, K Ravi-Chandar, Interaction of shear waves and propagating cracks. *Phys. Rev. Lett.* **91**, 235502 (2003).
18. D Bonamy, K Ravi-Chandar, Dynamic crack response to a localized shear pulse perturbation in brittle amorphous materials: on crack surface roughening. *Int. J. Fract.* **134**, 1–22 (2005).
19. M Wang, L Zhao, M Fourmeau, D Nelias, Crack plane deflection and shear wave effects in the dynamic fracture of silicon single crystal. *J. Mech. Phys. Solids* **122**, 472–488 (2019).
20. D Massy, et al., Crack front interaction with self-emitted acoustic waves. *Phys. review letters* **121**, 195501 (2018).
21. JW Morrissey, JR Rice, Crack front waves. *J. Mech. Phys. Solids* **46**, 467–487 (1998).
22. JW Morrissey, JR Rice, Perturbative simulations of crack front waves. *J. Mech. Phys. Solids* **48**, 1229–1251 (2000).
23. F Fekak, et al., Crack front waves: a 3d dynamic response to a local perturbation of tensile and shear cracks. *J. Mech. Phys. Solids*, 103806 (2019).
24. M Adda-Bedia, RE Arias, E Bouchbinder, E Katzav, Dynamic stability of crack fronts: out-of-plane corrugations. *Phys. review letters* **110**, 014302 (2013).
25. E Bouchaud, J Bouchaud, D Fisher, S Ramanathan, J Rice, Can crack front waves explain the roughness of cracks? *J. Mech. Phys. Solids* **50**, 1703–1725 (2002).
26. A Sagy, Z Reches, J Fineberg, Dynamic fracture by large extraterrestrial impacts as the origin of shatter cones. *Nature* **418**, 310 (2002).
27. E Sharon, G Cohen, J Fineberg, Propagating solitary waves along a rapidly moving crack front. *Nature* **410**, 68 (2001).
28. E Sharon, G Cohen, J Fineberg, Crack front waves and the dynamics of a rapidly moving crack. *Phys. Rev. Lett.* **88**, 085503 (2002).
29. J Fineberg, E Sharon, G Cohen, Crack front waves in dynamic fracture. *Int. J. Fract.* **121**, 55–69 (2003).
30. J Kermode, et al., Low-speed fracture instabilities in a brittle crystal. *Nature* **455**, 1224 (2008).

31. D Sherman, I Be'ery, From crack deflection to lattice vibrations—macro to atomistic examination of dynamic cleavage fracture. *J. Mech. Phys. Solids* **52**, 1743–1761 (2004).
32. MJ Buehler, H Tang, AC Van Duin, WA Goddard III, Threshold crack speed controls dynamical fracture of silicon single crystals. *Phys. Rev. Lett.* **99**, 165502 (2007).
33. L Zhao, D Bardel, A Maynadier, D Nelias, Crack initiation behavior in single crystalline silicon. *Scripta Materialia* **130**, 83–86 (2017).
34. L Zhao, D Bardel, A Maynadier, D Nelias, Velocity correlated crack front and surface marks in single crystalline silicon. *Nat. communications* **9**, 1298 (2018).
35. R Pratt, T Lim, Acoustic surface waves on silicon. *Appl. Phys. Lett.* **15**, 403–405 (1969).
36. G Wang, et al., Nanoscale periodic morphologies on the fracture surface of brittle metallic glasses. *Phys. review letters* **98**, 235501 (2007).
37. R Pérez, P Gumbsch, An ab initio study of the cleavage anisotropy in silicon. *Acta Materialia* **48**, 4517–4530 (2000).
38. F Atrash, D Sherman, Dynamic fracture instabilities in brittle crystals generated by thermal phonon emission: experiments and atomistic calculations. *J. Mech. Phys. Solids* **60**, 844–856 (2012).
39. J Willis, A Movchan, Three-dimensional dynamic perturbation of a propagating crack. *J. Mech. Phys. Solids* **45**, 591–610 (1997).
40. J Willis, A Movchan, The influence of viscoelasticity on crack front waves. *J. Mech. Phys. Solids* **49**, 2177–2189 (2001).
41. AN Norris, ID Abrahams, A multiple-scales approach to crack-front waves. *J. Eng. Math.* **59**, 399–417 (2007).
42. C Eckl, A Mayer, A Kovalev, Do surface acoustic solitons exist? *Phys. Rev. Lett.* **81**, 983 (1998).
43. G Perrin, JR Rice, Disordering of a dynamic planar crack front in a model elastic medium of randomly variable toughness. *J. Mech. Phys. Solids* **42**, 1047–1064 (1994).
44. JR Rice, Y Ben-Zion, KS Klm, Three-dimensional perturbation solution for a dynamic planar crack moving unsteadily in a model elastic solid. *J. Mech. Phys. Solids* **42**, 813–843 (1994).
45. D Nečas, P Klapetek, Gwyddion: an open-source software for spm data analysis. *Open Phys.* **10**, 181–188 (2012).